FEL SIMULATION USING THE LIE METHOD[*]

Kilean Hwang[†], Ji Qiang, Lawrence Berkeley National Laboratory, Berkeley, USA

Abstract

Advances in numerical methods for free-electron-laser (FEL) simulation under wiggler period averaging (WPA) are presented. First, WPA is generalized using perturbation Lie map method. The conventional WPA is identified as the leading order contribution. Next, a widely used shot-noise modeling method is improved along with a particle migration scheme across the numerical mesh. The artificial shot noise arising from particle migration is suppressed. The improved model also allows using arbitrary mesh size, slippage resolution, and integration step size. These advances will improve modeling of longitudinal beam profile evolution for fast FEL simulation.

INTRODUCTION

FEL design optimization often involve multiple times of numerical simulations with different system parameters. Such a study requires highly efficient simulation code. The WPA is the one of the best options. Indeed, most of the start-to-end design codes choose to incorporate the WPA FEL simulation code [1–5]. In this proceeding, we review the advances in numerical methods within the WPA framework presented in our previous work [6].

First, we generalize the WPA using the perturbation Lie map method. The conventional WPA is identified as the leading order contribution. The next order corrections we includes are coupling between betatron and wiggling motion, transverse field gradient, and longitudinal field envelope variation.

Second, we present an improved shot-noise model within WPA framework. Unless particle migration across the numerical mesh is artificially suppressed, as in many old WPA codes [7], there can be large artificial shot noise due to the nature of the shot-noise modeling method [8]. We solve this problem by re-interpreting and combining the two widely used shot-noise modeling methods of Refs. [8] and [9]. The improved modeling can further benefit smoothness of numerical mesh through arbitrary weight and shape functions. Here, the weight function refers to the integral kernel used for particle deposition on numerical mesh points. The shape function refers to the shape of the field representation at numerical mesh points used for field interpolation from mesh points to particles' coordinates. This, in turn, allows arbitrary mesh size, integration step size and slippage resolution. Especially, the arbitrary slippage resolution comes with many other benefits. It can naturally simulate correct slippage through non-resonant transport line other than wiggler and allows applying the operator split-composition method [10] on field solver for better accuracy. Last but the least, the particle loading method can naturally accept the particle data from upstream simulation enabling start-to-end simulation seamless.

GENERALIZATION OF WIGGLER PERIOD AVERAGING

In general, when a Hamiltonian can be decomposed into integrable part and a small parametric potential, one can build a perturbation map in order of the small parameters. In an undulator, if a map is constructed over a undulator period, the lowest order of the wiggling motion average out leaving the small coupling effects between the fast wiggling and slow betatron motion.

Magnus Series

We split the Hamiltonian into $H = S + F(z) + V(z)$ where S is the wiggler period averaged Hamiltonian representing slow motion, V is the radiation field potential, F is the rest representing the fast wiggling motion. Accordingly, we factor the Lie map as the following [11]:

$$
\begin{aligned}
\mathcal{H}(\lambda_u) &= \mathcal{S}(\lambda_u)\mathcal{F}(\lambda_u)\mathcal{V}(\lambda_u), \\
\mathcal{S}(\lambda_u) &= e^{\mathcal{G}_S(\lambda_u)}, \quad\quad (1) \\
\mathcal{F}(\lambda_u) &= e^{\mathcal{G}_F(\lambda_u)}, \quad\quad (2) \\
\mathcal{V}(\lambda_u) &= e^{\mathcal{G}_V(\lambda_u)},
\end{aligned}
$$

where λ_u is the wiggler period. The generators can be written in terms of the Magnus's series

$$
\begin{aligned}
\mathcal{G}_F(z) &= -\int_0^z dz_1 : F_1^{\text{int}}: +\frac{1}{2!}\int_0^z dz_1 \int_0^{z_1} dz_2 : [2,1]: \quad (3) \\
&\quad +\frac{1}{3!}\int_0^z dz_1 \int_0^{z_1} dz_2 \int_0^{z_2} dz_3 : [3,[2,1]] + [[3,2],1]: \\
\mathcal{G}_V(z) &= -\int_0^z dz : V^{\text{int}}(z): \quad\quad (4)
\end{aligned}
$$

where the pair of colons is Dragt's notation [11] of the Poisson bracket, i.e., $:A: B = [A, B]$, and the numbers in the Poisson bracket is an abbreviation of $i \equiv F_i^{\text{int}}$ with $F_i^{\text{int}} \equiv \mathcal{S}(z_i)F(z_i)$. Since the raidaiton field strength is much weaker than external field strength only the 1st sequence is taken for $\mathcal{G}_V$ [6].

Hamiltonian

Starting from the following Hamiltonian,

$$
H(\boldsymbol{x}, \boldsymbol{p}, ct, -\gamma; z) = -\sqrt{\gamma^2 - 1 - (p_x - a_x)^2 - (p_y - a_y)^2},
$$

where ct is the time multiplied by the speed of light and it's canonical momentum pair is negative of the normalized

---

energy $-\gamma$. The normalized vector potential of the planar wiggler is assumed to be

$$
\begin{aligned}
a_x &= K \cosh(k_x x)\cosh(k_y y)\cos(k_u z) + a_r, \\
a_y &= K\frac{k_x}{k_y}\sinh(k_x x)\sinh(k_y y)\cos(k_u z),
\end{aligned}
\tag{5}
$$

where k_u is the wiggler wave number, k_x and k_y are the natural focusing strength of the wiggler, K is the normalized wiggler strength. We use the following ansatz for the vector potential a_r

$$
a_r = \mathfrak{R}\sum_{h\geq 1} K_h(\boldsymbol{x},t;z)\,e^{ihk_r(z-ct)},
\tag{6}
$$

where, K_h is the h-th harmonic field envelope, and k_r is the fundamental wave number. The generating function,

$$
G_2(ct,\eta) = [k_r(z-ct)+k_u z]\eta
\tag{7}
$$

transforms the Hamiltonian into

$$
H = (k_u+k_r)\eta - \sqrt{k_r^2\eta^2 - 1 - (p_x-a_x)^2 - (p_y-a_y)^2},
$$

whose new conjugate variables are

$$
\theta \equiv k_r(z-ct)+k_u z, \qquad \eta \equiv \gamma/k_r.
\tag{8}
$$

Then, the split parts of the Hamiltonian are

$$
\begin{aligned}
S &\equiv \frac{k_u}{k_s}\gamma + \frac{1}{2\gamma}\left[1 + p_x^2 + p_y^2 + \frac{K^2}{2}\left(1 + k_x^2 x^2 + k_y^2 y^2\right)\right] \\
&\quad + \frac{K^2}{4\gamma}\left[\frac{1}{3}\left(k_x^4 x^4 + k_y^4 y^4\right) + k_x^2 k_u^2 x^2 y^2\right] \\
&\quad + \frac{1}{(2\gamma)^3}\left(1 + K^2 + \frac{3}{8}K^4\right) + O\left(\frac{q_\perp^6}{\gamma},\frac{q_\perp^2}{\gamma^3},\frac{1}{\gamma^5}\right),
\end{aligned}
\tag{9}
$$

$$
\begin{aligned}
F &\equiv \frac{K_{\text{eff}}^2}{4\gamma}\cos(2k_u z) + \frac{K_{\text{eff}}}{\gamma}p_x\cos(k_u z) \\
&\quad + O\left(\frac{q_\perp^3}{\gamma},\frac{1}{\gamma^3}\right),
\end{aligned}
\tag{10}
$$

$$
\begin{aligned}
V &\equiv -\mathfrak{R}\sum_h\left[\frac{K_{eff}}{\gamma}\cos(k_u z) + \frac{p_x}{\gamma}\right]K_h e^{ih(\theta-k_u z)} \\
&\quad + O\left(\frac{K_h q_\perp^2}{\gamma},\frac{K_h}{\gamma^3},\frac{K_h^2}{\gamma}\right),
\end{aligned}
\tag{11}
$$

where $q_\perp \in \{k_x x, p_x, k_y y, p_y\}$ and

$$
K_{\text{eff}} = K\left(1 + k_x^2\frac{x^2}{2} + k_y^2\frac{y^2}{2}\right)
\tag{12}
$$

is the effective wiggler strength.

Lie Map Generators

The generator of the slow map is trivial:

$$
\mathcal{G}_S(\lambda_u) = -\lambda_u :S:
\tag{13}
$$

Evaluating Eq. (3), the the fast map generator becomes

$$
\mathcal{G}_F(\lambda_u) = -\lambda_u\frac{K^4 k_x^2}{16 k_u^2\gamma^3}.
\tag{14}
$$

This corresponds to the coupling between slow betatron oscillation and fast wiggling oscillation. It is negligible in most cases as it scales as γ^{-2} compared to the wiggling motion in Eq. (10). The smallness is due to the large frequency ratio between the betatron and wiggling oscillation. When strong quadrupole is present on top of the wiggler field, such coupling can be more relevant.

Before we evaluate Eq. (4), let us write the propagated field potential $V^{\text{int}} \equiv \mathcal{S}\mathcal{F}V$ by

$$
V^{\text{int}} = -\left[\frac{K_{eff}}{\gamma}\cos(k_u z) + \frac{p_x}{\gamma}\right]K_h^{\text{int}}e^{ih(\theta^{\text{int}}-k_u z)},
\tag{15}
$$

where the real value operator and the summation over h is assumed for simplicity, and $K_h^{\text{int}} \equiv \mathcal{S}\mathcal{F}K_h$ and $\theta^{\text{int}} \equiv \mathcal{S}\mathcal{F}\theta$ are the propagated field envelope and FEL phase respectively. We neglected the propagation on terms in the square bracket of Eq. (15) assuming propagation on FEL phase and field envelope is more relevant.

In order to evaluate the integration in Eq. (4), we need to model the field envelope variation over the integration range. As the WPA presumes small field envelope variation over a wiggler period, we model as the following:

$$
K_h^{\text{int}}(z) = \mathbb{K}_h + \frac{K_{\text{eff}}}{k_u\gamma}\sin(k_u z)\frac{\partial}{\partial x}\mathbb{K}_h + z\partial_z\mathbb{K}_h,
\tag{16}
$$

where $\mathbb{K}_h = \frac{1}{z}\int_0^z K_h dz$ is an averaged field envelope, $\partial_z\mathbb{K}_h$ represent the first order longitudinal variation and the transverse gradient term is from the propagation by $\mathcal{F}(z)$. On the other hand, the propagated FEL phase is

$$
\theta^{\text{int}} = \theta + \dot\theta z - \xi\sin(2k_u z) - \zeta\sin(k_u z),
\tag{17}
$$

where

$$
\begin{aligned}
\dot\theta &\equiv k_u - \frac{k_r}{2\gamma^2}\left[1 + p_x^2 + p_y^2 + \frac{K_{\text{eff}}^2}{2}\right], \\
\xi &\equiv \frac{k_r K_{\text{eff}}^2}{8k_u\gamma^2}, \\
\zeta &\equiv \frac{k_r K}{k_u\gamma^2}p_x.
\end{aligned}
\tag{18}
$$

Note that $\dot\theta = 0$ exactly on resonance. The inclusion of it encompasses small off-resonant effects. Finally, the generator of the field potential map can be written by

$$
\mathcal{G}_V = \lambda_u\mathfrak{R}\sum_h\frac{e^{ih\theta}}{\gamma}
\tag{19}
$$

$$
\times\left[K_{\text{eff}}\int_C^h + p_x\int_1^h + K\int_{zC}^h\partial_z + \frac{K_{\text{eff}}^2}{k_u\gamma}\int_{SC}^h\partial_x\right]\mathbb{K}_h,
$$

where the integration parameters are [6]:

$$\int_C^h = \frac{1}{2}\left(J_{-\frac{h-1}{2}}^{h\xi_R} + J_{-\frac{h+1}{2}}^{h\xi_R}\right)\left(1 + \frac{ih\dot\theta\lambda_u}{2}\right) - \frac{1}{2}\frac{h\dot\theta}{k_u}\left(\sum_{l\neq -\frac{h-1}{2}}\frac{J_l^{h\xi_R}}{(2l+h-1)} + \sum_{l\neq -\frac{h+1}{2}}\frac{J_l^{h\xi_R}}{(2l+h+1)}\right)$$

$$- \frac{1}{2}\Delta\xi\left(\frac{h-1}{2\xi_R}J_{-\frac{h-1}{2}}^{h\xi_R} + hJ_{-\frac{h-3}{2}}^{h\xi_R} + \frac{h+1}{2\xi_R}J_{-\frac{h+1}{2}}^{h\xi_R} + hJ_{-\frac{h-1}{2}}^{h\xi_R}\right) + \frac{h\zeta}{2}\frac{1}{2}\left(J_{-\frac{h+2}{2}}^{h\xi_R} - J_{-\frac{h-2}{2}}^{h\xi_R}\right), \quad (20)$$

$$\int_1^h = J_{-\frac{h}{2}}^{h\xi_R}\left(1 + \frac{ih\dot\theta\lambda_u}{2}\right) - \frac{h\dot\theta}{k_u}\sum_{l\neq -\frac{h}{2}}\frac{J_l^{h\xi_R}}{(2l+h)} - \Delta\xi\left(\frac{h}{2\xi_R}J_{-\frac{h}{2}}^{h\xi_R} + hJ_{-\frac{h}{2}+1}^{h\xi_R}\right) + \frac{h\zeta}{2}\left(J_{-\frac{h+1}{2}}^{h\xi_R} - J_{-\frac{h-1}{2}}^{h\xi_R}\right), \quad (21)$$

$$\int_{zC}^h = \frac{\lambda_u}{4}\left(J_{-\frac{h-1}{2}}^{h\xi_R} + J_{-\frac{h+1}{2}}^{h\xi_R}\right) + \frac{i\lambda_u}{4\pi}\left(\sum_{l\neq -\frac{h-1}{2}}\frac{J_l^{h\xi_R}}{(2l+h-1)} + \sum_{l\neq -\frac{h+1}{2}}\frac{J_l^{h\xi_R}}{(2l+h+1)}\right), \quad (22)$$

$$\int_{SC}^h = \frac{1}{4i}\left(J_{-\frac{h-2}{2}}^{h\xi_R} - J_{-\frac{h+2}{2}}^{h\xi_R}\right). \quad (23)$$

Here, the integration parameters are calculated to the first order of $\dot\theta$, ζ, $\Delta\xi \equiv \xi - \xi_R$ with $\xi_R \equiv \frac{k_r K^2}{8k_u\gamma_R^2}$ and γ_R being the resonant energy. The first kind Bessel function of order i and argument $h\xi_R$ is abbreviated as $J_i^{h\xi_R}$ and only integer i is allowed. Note that the integration parameter $\int_{SC}$ coupled with the transverse gradient in Eq. (19) vanishes for odd harmonics but can be as large as the leading order terms for even harmonics.

Effective Hamiltonian

The factorized map Eq. (2) is not yet practically useful for numerical implementation since each factorized map is not solvable and the step size is fixed by one wiggler period. A trick is to concatenate the map using Baker-Campbel-Hausdorff (BCH) formula and define an effective Hamiltonian [11],

$$H_{\text{eff}} = -\frac{1}{\lambda_u}(\mathcal{G}_S + \mathcal{G}_F + \mathcal{G}_V) \quad (24)$$

$$- \frac{1}{2\lambda_u}(:\mathcal{G}_S:\mathcal{G}_F + :\mathcal{G}_S:\mathcal{G}_V + :\mathcal{G}_F:\mathcal{G}_V) + \dots$$

Note that the effective Hamiltonian does not have explicit dependency on z. Therefore, we can apply numerical methods like Runge-Kutta (RK) with arbitrary step size to solve the effective Hamiltonian. For example, a popular FEL simulation code GENESIS uses the 4th order RK method [7]. Figure 1 shows an order of magnitude improvement in accuracy of particle pusher compared to the conventional WPA. We used the GENESIS pusher to represent typical WPA. Since, we used converging small enough step sizes, the error from the exact solution originate from the differences of the effective equations of motion in use. However, such an accuracy improvement on particle pusher can easily become obscured by other source of errors such as paraxial approximation of field solver, and numerical discretization.
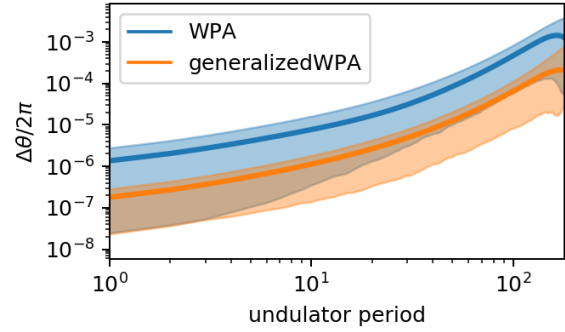
Figure 1: Comparison of particle pushers derived from Lie map and conventional WPA. The error is defined by $\Delta\theta \equiv |\theta - \theta_{\text{ref}}|$ where θ_{ref} is from a converging small enough step size integration of exact Hamiltonian and the two θ are from the 4th order RK tracking of the conventional WPA and the generalized WPA. Exponentially growing gaussian field envelope from 0.4 MW to 1 GW in power, $\sigma_r = 56\,\mu$m and $\lambda_r = 27$ nm is assumed. Electron beam parameters used are $\sigma_{x,y} = 56\,\mu$m, $\epsilon_{x,y} = 0.6\,\mu$m, $\gamma = 1000$ and $\Delta\gamma/\gamma = 2\times 10^{-4}$. Wiggler parameters used are $K = 1.5$, $\lambda_u = 2.5$ cm, and $k_x = k_y = k_u/\sqrt{2}$. The thick line represents the average and the shadowed area corresponds to the range of error of simulated particles' population.

NUMERICAL SHOT NOISE MODELING

Review of 1D Model

Here, we review two widely used 1D shot noise modeling methods in Ref. [8] and [9]. Figure 2 illustrates these two methods schematically. In both methods, the first step is to populate particles uniformly along the temporal coordinate with equal charge weight to remove artificial temporal shot-
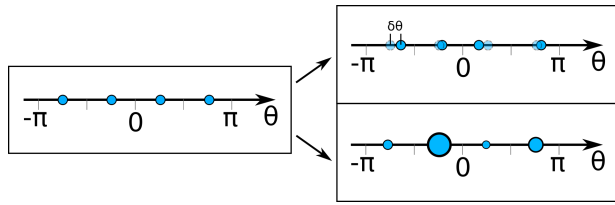
Figure 2: Schematic description of the 1D shot-noise modeling methods. Unperturbed uniform particle loading on left. Temporal coordinate perturbation on the upper right. Charge weight perturbation on the lower right.

noise. The bunching factor at this step is

$$b_h^0 = \frac{1}{N_e} \sum_{j=1}^{M} m_j e^{ih\theta_j} = 0. \qquad (25)$$

Here, index 0 denotes vanishing bunching factor, N_e is the number of electrons, M is the number of the simulated particles and $m_j = N_e/M$ is the electron number weight of the j-th particle. It vanishes as all the weights are equal, and the temporal coordinates $\theta_j = \theta_0 + j\Delta\theta$ are uniformly distributed with a equal distance $\Delta\theta = 2\pi/M$.

The second step is to add proper perturbation on the temporal coordinates or charge weights so that, at least, the root-mean-square (RMS) bunching factor is that of physical shot-noise $\langle b_h b_h^* \rangle = 1/N_e$.

The perturbation on temporal coordinate of j-th particle is given by [8]

$$\delta\theta_j \equiv \sum_{h'=1}^{M/2} \xi_{h'} e^{-ih'\theta_j}, \qquad (26)$$

where the number of particles is assumed to be twice of the maximum harmonic number to be modeled and ξ_h is a random variable. Then, the bunching factor becomes

$$b_h = \frac{1}{N_e} \sum_{j=1}^{M} m_j e^{ih(\theta_j + \delta\theta_j)} \simeq ih\xi_h. \qquad (27)$$

Therefore, we require $\langle \xi_h \xi_h^* \rangle = 1/(h^2 N_e)$ so that

$$\langle b_h b_h^* \rangle \simeq h^2 \langle \xi_h \xi_h^* \rangle \equiv \frac{1}{N_e}. \qquad (28)$$

On the other hand, when the charge weight perturbation [9] is applied, the RMS bunching factor becomes

$$\langle b_h b_h^* \rangle = \frac{1}{N_e^2} \sum_j^M \sum_k^M \langle \tilde{m}_j \tilde{m}_k \rangle e^{ih(\theta_j - \theta_k)} \qquad (29)$$

$$= \frac{1}{N_e^2} \sum_j^M \left(\langle \tilde{m}_j^2 \rangle - \langle \tilde{m}_j \rangle^2 \right) = \frac{1}{N_e}, \qquad (30)$$

where $\tilde{m}_j \equiv m_j + \delta m_j$ is the perturbed number weight with

$$\langle \tilde{m}_j \rangle = \langle \tilde{m}_j^2 \rangle - \langle \tilde{m}_j \rangle^2 = \frac{N_e}{M}. \qquad (31)$$

Note that this is a property of the Poisson distribution [9].

Review of 6D Extension

One way to extend the 1D shot-noise method is the 6D volume division method. This is a natural extension of the 1D charge perturbation based on Poisson principle. Density function is represented by particles sitting at the center of each 6D volume division. As each volume does not overlap, all the particles are statistically independent. However, it requires a lot of particles as division over 6 dimension can be huge.

Another way is to mirror same 5D coordinates x, y, p_x, p_y, γ among a set of particles called 'beamlet' [8] which models 1D shot-noise. Note that the member particles of a beamlet are not statistically independent as they share the same 5D phase-space coordinates. However, there can be large numerical shot-noise upon particles migration across the numerical mesh. This is because, the migration break the cancellation of bunching factor in Eq. (25).

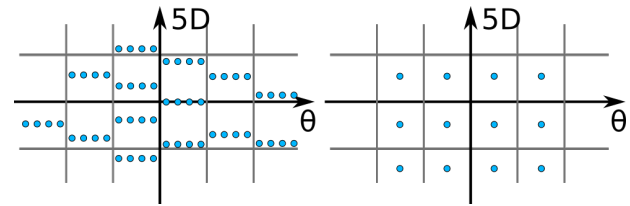Figure 3 illustrates these two 6D extension methods schematically.

Figure 3: Schematic description of the 6D extension methods of the 1D shot-noise modeling methods. The 5D mirroring method on the left and the 6D volume division method on the right.

Particle Loading and Migration

As the 6D volume division requires a lot of particles, we adopt the 5D mirroring strategy. Our idea is to interpret one beamlet as one statistically independent entity whose phase-space coordinate is given by the average over the member particles in it. This is based on the observation that the member particles are not statistically independent and the motion of the beamlets describe the macroscopic ($\gtrsim \lambda_r$) dynamics while the motion of the individual member particles of the beamlet describe microscopic ($\lesssim \lambda_r$) dynamics.

This interpretation allows us to load particles naturally. First, the beamlet is loaded from a random generator or from external upstream tracking code. Then, each beamlet is divided into $M = 2h_{max}$ particles whose temporal coordinates and charge follows the 1D shot-noise model while the average coordinate is that of the beamlet. Here h_{max} is the maximum harmonic number to be modeled. This procedure is described in Fig. 4.

Since the beamlet is an independent entity, we migrate all the particles composing a beamlet when the beamlet migrate across the numerical mesh. This method grants us much smoother numerical discretization as the weight and shape functions are evaluated at the beamlet position regardless
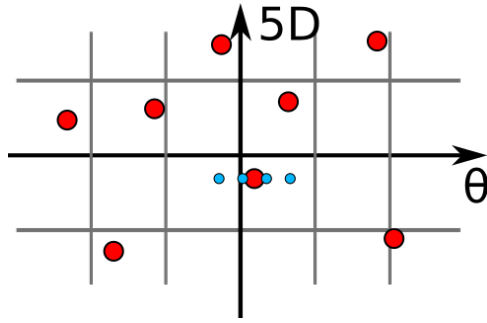
Figure 4: Schematic illustration of beamlets (red) and member particles (blue) composing a beamlet.

of individual member particle's relative coordinates. Figure 5 presents a benchmark between the beamlet migration and GENESIS v.1.3 in Self Amplified Spontaneous Eemission (SASE) simulation showing a good agreement between the two codes. However, there can be significant deviation from correct model when the artificial shot-noise due to individual particle migration dominate initial emission as shown in Fig. 6.
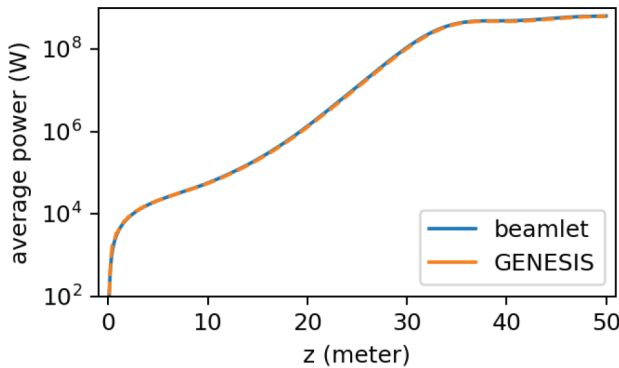

Figure 5: Bench mark between GENESIS v.1.3 and beamlet migration of SASE simulation using Next Generation Light Source (NGLS) parameters [12]. Blue is the beamlet migration. Dashed orange is GENESIS v.1.3
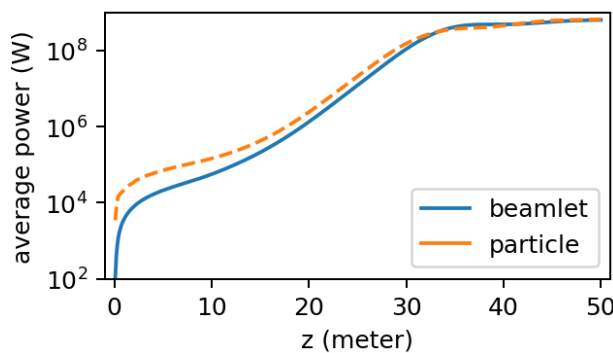

Figure 6: Illustration of artificial shot-noise due to particle migration. Same parameters used as in Fig. 5. Blue is from the beamlet migration. Dashed orange is from the individual particle migration.

SLIPPAGE RESOLUTION

The beamlet migration enables us to use arbitrary slippage resolution through moving window. The typical implementation of slippage is to copy the field data from the previous temporal mesh point to the next temporal mesh point. This procedure as well as the moving window can be best understood by a pseudo code in Fig. 7. Note that the slippage

```
Data Copy from previous slice
for i in [0,1,2,...,nt]:
    Fld.data[:,:,nt-i] = Fld.data[:,:,nt-i-1]
```

```
Moving wondow : change of domain
Fld.domain.theta[:]
  = Fld.domain.theta[:]+dtheta
```

Figure 7: Pseudo code illustrating slippage implementation of the copying data and the moving window. The first two indices of Fld.data are for the transverse mesh points while the last index is for the temporal mesh point. Here, nt is the number of temporal mesh points. The domain range represented by Fld.domain is used by deposition and interpolation algorithm. Therefore, change of the domain range by dtheta effectively slip the field by dtheta.

resolution of the moving window is arbitrary while the slippage resolution of the copying data is one temporal mesh size. Furthermore, moving window with beamlet migration can naturally and correctly model the slippage through arbitrary length of non-resonant transport like drift. Figure 8 shows kinks on power gain curve due to rough slippage resolution for the copying data. The power difference is especially notable in the drift-quadrupole line.

SPLIT AND COMPOSITION METHOD IN FIELD SOLVER

The field solver can be split into two operation - diffusion and slippage. Let $\mathcal{F}_\perp$ and $\mathcal{F}_\parallel$ represent the diffusion and slippage operator respectively. Then, the following composition method of step size Δz,

$$\mathcal{F}_\parallel \left(\frac{\Delta z}{2} \right) \mathcal{F}_\perp (\Delta z) \mathcal{F}_\parallel \left(\frac{\Delta z}{2} \right) \qquad (32)$$

is a second order method provided that $\mathcal{F}_\perp$ and $\mathcal{F}_\parallel$ are one-step method of order higher than two [10]. The arbitrary slippage resolution though moving window allow us to split $\mathcal{F}_\parallel$ and build the 2nd order composition method. Figure 9 shows comparison of the power gain curve error using the 1st order the 2nd order method.

CONCLUSION

Several advances in numerical methods for FEL simulation under the WPA are presented. We generalized the WPA using the perturbation Lie map method. The perturbative correctional terms to WPA includes coupling between fast
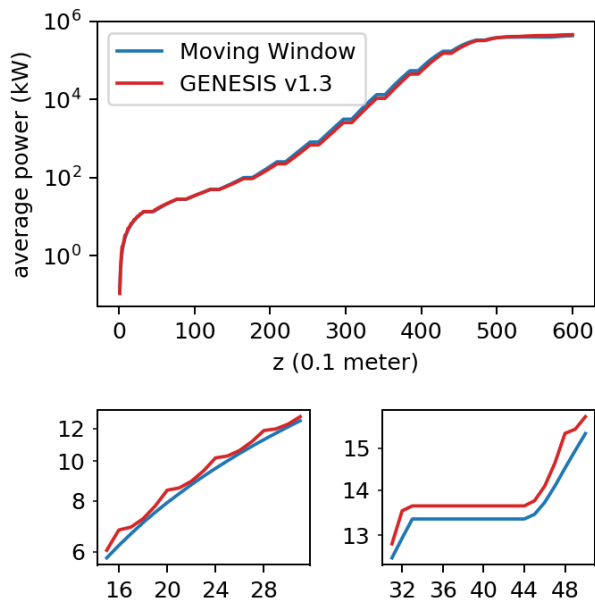
Figure 8: Effect of slippage resolution on power gain curve. Similar parameters are used as Fig. 6. except that drift and quadrupole elements are added here. The integration step size is 5 wiggler period (=0.1 m) and the temporal mesh size is 20 wavelength. The moving window is compared with `GENESIS v.1.3` which uses the copying data for field slip.
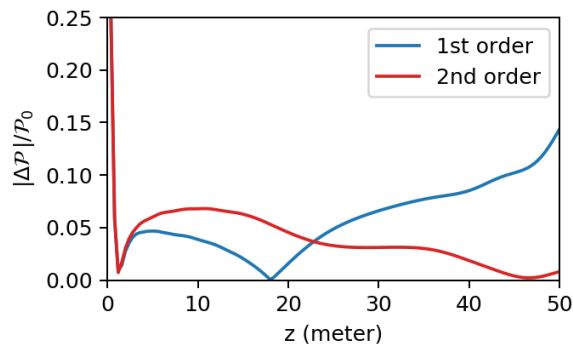

Figure 9: Comparison of the convergence between the two integration orderings. $\mathcal{P}_0$ is the reference power curve, $\Delta\mathcal{P}$ is the difference between the power curve simulated with a large step size($\Delta z = 20\lambda_u$) and the reference curve. Same parameters are used as Fig. 6. The large deviation at the initial stage is due to shot-noise.

wiggling and slow betatron motion, transverse field gradient, and longitudinal field variation. In addition, we improved the shot-noise modeling method. This allows us to combine advantages of two widely used shot-noise modeling methods in Refs. [8] and [9]. Such an improvement also leads us to develop a particle migration scheme suppressing artificial shot-noise upon migration. This enables much smoother numerical discretization and the temporal beam profile evolution modeling. All these methods are implemented in the parallel beam dynamics simulation framework IMPACT code suite [13].

ACKNOWLEDGEMENTS

REFERENCE

[1] S. Reiche, C. Pellegrini, J. Rosenzweig, P. Emma, and P. Krejcik, "Start-to-end simulation for the LCLS X-ray FEL", *Nucl. Instrum. Methods Phys. Res., Sect. A*, vol. 483, pp. 70–74, 2002.

[2] M. Dohlus, K. Flottmann, O. S. Kozlov, T. Limberg, Ph. Piot, E. L. Saldin, E. A. Schneidmiller, and M. V. Yurkov, "Start to end simulations of SASE FEL at the TESLA Test Facility. Phase 1", *Nucl. Instrum. Meth., Sect. A*, vol. 530, pp. 217–233, 2004.

[3] Y. Ding *et al.,* "Start-to-End Simulations of the LCLS Accelerator and FEL Performance at Very Low Charge", *Proc. PAC'09*, Vancouver, Canada, 2009, paper WE5RFP040

[4] J. Qiang *et al.,* "Start-to-End Simulation of the LCLS-II Beam Delivery System with Real Number of Electrons", *Proc. FEL2015*, Daejeon, Korea, 2015, paper WEP070

[5] J. Qiang, Y. Ding, P. Emma, Z. Huang, D. Ratner, T. O. Raubenheimer, M. Venturini, and F. Zhou, "Start-to-end simulation of the shot-noise driven microbunching instability experiment at the Linac Coherent Light Source", *Phys. Rev. Accel. Beams*, vol. 20, pp. 054402, 2017.

[6] K. Hwang, J. Qiang, "Advances in numerical methods under wiggler period averaging for free electron laser simulation", *Phys. Rev. Accel. Beams* (submitted in 2018).

[7] S. Reiche, "GENESIS 1.3: A fully 3D time-dependent FEL simulation code", *Nucl. Instrum. Methods Phys. Res., Sect. A*, vol. 429, p. 243, 1999.

[8] William M. Fawley, *Phys. Rev. ST Accel. Beams*, vol. 5, pp. 070701, 2002.

[9] B. W. J. McNeil, M. W. Poole, and G. R. M. Robb, *Phys. Rev. ST Accel. Beams*, vol. 6, pp. 070701, 2003.

[10] E. Hairer, C. Lubich, and G. Wanner, *Geometric Numerical Integration*, Springer, 2006.

[11] Alex J. Dragt, "Lie Methods for Nonlinear Dynamics". http://www.physics.umd.edu/dsat/dsatliemethods.html

[12] J. Qiang, J. Corlett, C. E. Mitchell, C. F. Papadopoulos, G. Penn, M. Placidi, M. Reinsch, R. D. Ryne, F. Sannibale, C. Sun, M. Venturini, P. Emma, and S. Reiche, "Start-to-end simulation of x-ray radiation of a next generation light source using the real number of electrons", *Phys. Rev. ST Accel. Beams*, vol. 17, pp. 030701, 2014.

[13] J. Qiang, R. Ryne, S. Habib, and V. Decyk, *J. Comp. Phys.*, vol. 163, pp. 434, 2000.